International Journal of Safety and Security Engineering
Vol. 16, No. 3, March, 2026, pp. 691-700
Journal homepage: http://iieta.org/journals/ijsse

Effect of Surface Roughness on Mechanical and Fatigue Performance of Ultra-Thin 304 Stainless Steel Sheets

Ammar Adil Al-Bakri, Raed A.M. Al-Mamoori, Haider F. Mahmood*

Al-Mussaib Technical College, Al-Furat Al-Awsat Technical University, Babylon 51006, Iraq

Corresponding Author Email: haider.fawzi@atu.edu.iq

https://doi.org/10.18280/ijsse.160319

Received: 6 February 2026
Revised: 11 March 2026
Accepted: 18 March 2026
Available online: 31 March 2026

Keywords:
surface roughness, ultra-thin 304 stainless steel, fatigue behavior, mechanical properties, crack initiation mechanisms, S–N curve, surface integrity

ABSTRACT

This study investigates the influence of surface roughness on the mechanical and fatigue properties of ultra-thin 304 stainless steel sheets through an integrated approach. Six different surface conditions were produced using mechanical and chemical treatments, with arithmetic average roughness values ranging from 0.05 to 2.01 μm. The impact of surface roughness on material characteristics under applied loads was assessed using tensile and high-cycle fatigue tests. The findings indicate that heightened surface roughness resulted in diminished yield strength, ultimate tensile strength (UTS), ductility, and fatigue limit. The fatigue response exhibits higher sensitivity compared to tensile properties. A decreasing trend in fatigue limit with increasing surface roughness is observed. Fractographic analysis reveals a transition in fatigue crack initiation from subsurface inclusion-controlled mechanisms to surface irregularity-dominated mechanisms with increasing roughness.

1. INTRODUCTION

Ultra-thin metallic sheets are commonly used in modern advanced engineering applications such as microelectronic devices, biomedical devices, aerospace structures, and microelectromechanical devices/systems, where high strength-to-weight ratios and reliable mechanical properties are critical. Among such metallic sheets, type 304 austenitic stainless steel has been found to be a popular choice owing to its high corrosion resistance, good formability, and desirable mechanical properties. With the increasing tendency for miniaturization and downscaling of products, it has now become imperative to evaluate the mechanical properties of ultra-thin stainless steel sheets for ensuring reliable mechanical performance.

Surface roughness has been identified as a critical factor that influences the mechanical behavior of metallic sheets, particularly ultra-thin metallic sheets, as their surface-to-volume ratio is substantially higher than that of conventional metallic materials. Manufacturing operations such as rolling, grinding, polishing, and chemical etching always result in surface irregularities that can be treated as geometric discontinuities. The surface roughness phenomenon can be classified into form errors at the macro-scale, waviness at the meso-scale, and surface roughness at the micro-scale, as described in the study [1]. Of particular interest to engineering applications are surface micro-roughness, as it has a direct influence on mechanical properties.

Surface roughness is usually specified using statistical parameters obtained from profile measurements. The arithmetic average roughness (Ra) is still the most commonly used roughness parameter owing to its simplicity and ease of measurement [2, 3]. Nevertheless, it is not sufficient to define the functionality of a surface because it has been found that surfaces with the same Ra may have very different topographies [4]. In this regard, other roughness parameters such as Rq, Rz, Rsk, and Rku have been used to define the surface characteristics [5]. The development of advanced techniques for characterizing surfaces has allowed the 3D characterization of surfaces using techniques such as atomic force microscopy, confocal microscopy, and white light interferometry [6]. The 3D roughness parameters have been found to better relate to the functional performance of a surface compared to two-dimensional parameters [7, 8].

The effect of surface roughness on the mechanical properties of bulk metallic materials has been widely studied. The increase in surface roughness has been observed to affect the tensile strength and ductility of metallic materials due to stress concentration effects [9, 10]. The effect of surface roughness is seen to be more significant in metallic sheets of smaller thickness since the dimensions of surface roughness can be of the same order of magnitude as the sheet thickness. Experiments were performed on ultra-thin copper and aluminum sheets, and significant effects of surface roughness were observed in reducing the yield strength and ductility of the metallic materials [11, 12].

The effect of surface roughness is seen to be even more significant in the fatigue behavior of metallic materials since the initiation of fatigue cracks usually takes place around surface irregularities. The effect of surface roughness in ultra-thin metallic sheets is still not understood, and several studies were performed to understand its effect on the fatigue behavior of metallic materials. The existing models of ultra-thin metallic materials were observed to indicate that increased surface roughness leads to increased stress concentration and decreased fatigue strength [13-15].

Fatigue crack initiation mechanisms are heavily dependent on surface and microstructural features. In the case of smooth surfaces, the crack initiation mechanism is dominated by subsurface inclusions or microstructural heterogeneities, especially in high-cycle fatigue [16-19]. As the roughness of the surface increases, the crack initiation mechanism is dominated by surface features, which act as stress concentrators and induce localized plastic deformation [20, 21]. In severe cases, several fatigue cracks can occur simultaneously at the surface, and there can be an interaction between the fatigue cracks, which can reduce fatigue life [22]. Extreme cases may experience the initiation of multiple fatigue cracks simultaneously on the surface, which may interact with each other and reduce the fatigue life [22]. The crack initiation process for sheet materials may also become complicated by the interaction between the surface roughness and the microstructural properties, such as the grain size, which may cause the crack initiation mode to change from crystallographic to non-crystallographic [23, 24].

Type 304 stainless steel is known to have a face-centered cubic microstructure with excellent ductility and corrosion resistance but is also known to be susceptible to work hardening and strain-induced martensitic transformation under severe deformation [25]. Previous studies on Type 304 stainless steel have been limited to its corrosion and fatigue properties, mostly on conventional thick materials. Smoothening the surface of Type 304 stainless steel is known to improve its corrosion and fatigue properties, especially due to the reduction in surface defects [26-29]. Although previous studies have been conducted on the mechanical and fatigue properties of ultra-thin Type 304 stainless steel sheets, the influence of surface roughness on the mechanical and fatigue properties of the material is still unclear, especially since previous studies on thin sheets or foils have been limited to size effects, with little or no attention given to the influence of surface roughness on the mechanical and fatigue properties [30, 31].

Based on the literature, the following research gaps can be identified:

- The effect of surface roughness on the mechanical and fatigue properties of ultra-thin 304 stainless steel sheets is still unknown, although there are some studies on quantifying the effect of surface roughness on the mechanical and fatigue properties of metallic sheets.
- The transition of fatigue crack initiation mechanisms with increasing surface roughness of metallic sheets is still unknown.
- Quantitative models correlating surface roughness parameters to fatigue performance, considering size effect and stress concentration effect, are still inadequate.
- The relationship between surface topography and stress concentration factors is still unknown, especially when the surface features are 3D.

2. MATERIALS AND METHODS

2.1 Material preparation

Commercially available sheets of 304 austenitic stainless steel were used. These sheets were of nominal thickness 0.2 mm. Solution annealed material was used for this work. Chemical composition of the material by optical emission spectroscopy indicated that the material consisted of approximately 18.5% Cr, 8.5% Ni, 1.8% Mn, 0.42% Si, 0.05% C, 0.03% P, 0.002% S, and the balance Fe.

To relieve residual stresses and to obtain a microstructure as homogeneous as possible, solution annealing of the material at 1050 °C for 30 minutes followed by water quenching was carried out. Average grain size of the material after heat treatment was determined to be 45 ± 5 μm by linear intercept method in accordance with ASTM E112.

Six different surface conditions were created by a series of controlled mechanical polishing and chemical etching operations. Before any specific surface condition is created on any specimen, all specimens were subjected to sequential grinding operations using different grit sizes of SiC abrasive papers ranging from P180 to P4000 to create a baseline surface condition. After creating this baseline surface condition, different final surface conditions were created as follows:

- **S1 (Mirror Polished)**: All specimens had a mirror finish after mechanical polishing with diamond suspensions of decreasing particle sizes (6, 3, 1, 0.25, and 0.05 μm) and colloidal silica.
- **S2 (Fine Polished)**: Mechanical polishing was carried out with diamond suspensions up to 1 μm in particle size.
- **S3 (Standard Polished)**: Mechanical polishing was stopped at 3 μm diamond suspension.
- **S4 (Fine Ground)**: The specimens were ground using SiC paper up to the grit size of P2000.
- **S5 (Coarse Ground)**: Samples were grounded with sandpaper up to P800 grain size.
- **S6 (Chemically Etched)**: Specimens were ground down to P800 using grinding paper and then etched in 10% HNO_3, 20% HCl, and 70% H_2O by volume for 60 seconds at room temperature.

After creating different surface conditions on different specimens, ultrasonic cleaning of all specimens in acetone for 15 minutes followed by ultrasonic cleaning in ethanol for 10 minutes and then drying in warm air was carried out.

It should be noted that although the six surface conditions were primarily designed to represent different levels of surface roughness, the applied surface preparation routes (mechanical polishing, grinding, and chemical etching) may also introduce variations in near-surface microstructure. These may include plastic deformation gradients, residual stresses, and strain-induced martensitic transformation, as confirmed in Sections 2.2 and 3.1. Therefore, the observed mechanical and fatigue responses should be interpreted as the combined effect of surface topography and subsurface metallurgical state, rather than roughness alone.

2.2 Surface characterization

2.2.1 Surface roughness measurements

Surface roughness measurements were performed using a digital stylus profilometer (S202, Grasbry & Cubiaco Inc., Switzerland). For each surface condition, ten profiles were recorded at random orientations with a scan length of 5 mm, a stylus force of 3 mg, and a lateral resolution of 0.33 μm. The measured profiles were filtered using a Gaussian filter with a cutoff wavelength of 0.8 mm in accordance with ISO 4287 to separate roughness from waviness.

3D surface topography was evaluated using a white-light interferometer (Zygo NewView 7300) with a vertical resolution of 0.1 nm and a lateral resolution of 0.5 μm. Five measurements were obtained at random locations on each specimen over an area of 1.2 mm × 0.9 mm. Areal roughness parameters were calculated in accordance with ISO 25178 using MetroPro software. The evaluated parameters included Ra/Sa, Rq/Sq, Rz/Sz, Rsk/Ssk, and Rku/Sku.

2.2.2 Microstructural analysis

The surface and near-surface microstructures of the material have been characterized using a field-emission scanning electron microscope (FE-SEM) (JEOL JSM-7600F) with an accelerating voltage of 15 kV. The secondary electron imaging mode was used to examine the surface morphological features of the material. The backscattered electron imaging mode was used to examine the grain structure of the material.

The phase composition of the material has been characterized using an X-ray diffractometer (Rigaku SmartLab) with Cu Kα radiation of wavelength 0.15406 nm. The diffractometer was operated at an accelerating voltage of 40 kV and a current of 44 mA. The diffractometer was scanned from $2\theta = 30°$ to 100° with a step size of 0.025°. The scanning speed was set to 2 seconds/step. The residual stress has been evaluated using the $\sin^2\psi$ method.

The near-surface deformation of the material has been characterized using an electron backscattered diffraction (EBSD) technique. The EBSD technique has been used to examine the orientation of grains of the material. The EBSD pattern has been obtained using an Oxford Instruments Nordlys Nano detector attached to the FE-SEM. The step size of the EBSD pattern was set to 0.2 μm. The orientation of grains of the material has been analyzed using AZtec software. The presence of strain-induced martensitic transformation has been evaluated using AZtec software.

2.3 Mechanical testing

2.3.1 Tensile testing

Uniaxial tensile tests were carried out based on the ASTM standard E8/E8M. Miniature dog-bone specimens with a gauge length of 25 mm and width of 6 mm were utilized. The specimens were cut from the prepared sheets using a wire electrical discharge machining technique to reduce edge effects. The tensile tests were carried out using an Instron 5967 universal test machine at a constant crosshead speed of 10 mm/min. The strain was recorded using a non-contact video extensometer. All experiments were carried out at ambient temperature, i.e., 23 ± 2 ℃. Five specimens were tested for each surface condition. The following mechanical properties were extracted from stress-strain curves: Young’s modulus, 0.2% offset yield strength, ultimate tensile strength (UTS), uniform elongation, total elongation, and strain-hardening exponent.

2.3.2 Fatigue testing

High cycle fatigue tests were carried out on an Instron ElectroPuls E10000 electrodynamic testing system. The tests were carried out under load control. The specimens were tested at a stress ratio $R = 0.1$, tension-tension, and a frequency of 20 Hz. Various stress levels were used to generate complete S-N diagrams. The run-out criterion used was 10^7. For every surface, a minimum of twelve specimens were tested, including multiple stress levels within the finite life regime and additional tests near the fatigue limit to verify the fatigue properties. The experiments were carried out in uniform environmental conditions at a temperature of 23 ± 2 ℃ and relative humidity of 45 ± 5%. The fatigue ratio was defined as the ratio of fatigue strength to UTS.

In the fatigue test, the test matrix consisted of a variety of stress levels, which were represented in terms of percentages of UTS. It ranged from 90 to 40 percent UTS. For each surface condition, a minimum of two to three specimens were tested at each stress level. Fatigue limit was determined around 10^7 cycles, and the staircase approach was used, in which the specimens' stress amplitude was altered according to the results obtained from the previous specimens.

Run-out specimens (i.e., specimens surviving 10^7 cycles) were included in the analysis and treated as censored data during S-N curve fitting.

S-N curves were fitted using a log-log linear regression based on Basquin’s relation.

2.3.3 Fractography

The fracture surfaces of tensile and fatigue specimens were investigated using field emission scanning electron microscopy to determine the fracture features and crack initiation sites. For the fatigue specimens, particular attention was given to distinguishing between surface-initiated and subsurface-initiated cracks, and to understanding the behavior of the crack at its initiation stage.

Some of the fracture surfaces were investigated using a dual beam FIB tool, specifically FEI Quanta 3D FEG, to perform cross-sectioning of the fracture surfaces. Energy-dispersive X-ray spectroscopy (EDS) was used to determine if there were any inclusions that could have led to crack initiation.

2.4 Finite element analysis

Finite element analysis (FEA) was conducted to measure the effects of the stress concentrations due to surface roughness. The surface profile, which was measured using a stylus profiler, was imported into the ABAQUS 2019 software to create a numerical model. A two-dimensional plane strain numerical model was created to simulate tensile and fatigue loading conditions.

The material behavior of the surfaces was modeled using an elastic-plastic material model, considering isotropic hardening, based on experimental stress-strain data. The boundary conditions were selected based on the experimental conditions. The numerical models were validated by conducting a mesh sensitivity analysis, where the minimum mesh size was selected based on the stress gradient at the surface.

The numerical models were used to investigate the local stress-strain distribution around the surface. The stress concentration factors were calculated using the numerical models. In addition, 3D models were developed for some of the surfaces based on the topographical data measured using optical interferometry, considering the same material behavior and boundary conditions, to investigate the effect of 3D surface features on stress concentration.

2.5 Statistical analysis

Statistical processing of data was done with IBM SPSS Statistics 26 software. Analysis of variance (ANOVA) was implemented to test the significance of differences in mechanical properties due to differences in surface roughness and the Tukey’s HSD test was used for comparisons between specific conditions. Linear regression was used as a technique to identify quantitative relationships between roughness parameters and performance properties with correlation coefficients (R^2) where appropriate judgments on the strength of these relations. Furthermore, multiple regression analyses were carried out with R^2 to determine which combination of roughnesses best predicted performance. The standard errors of the regression parameters were also evaluated.

All reported values represent the mean ± standard deviation. Statistical significance was evaluated at a confidence level of 95% ($p < 0.05$).

2.6 Predictive model development

Based on the experimental results and the FE, this study proposed a predictive fatigue model that includes the influence of surface roughness on the fatigue life of materials. In the proposed model, the Basquin equation is revised as follows:

$$\sigma_a = C_1 (N_f)^{-C_2} f(R_a) \tag{1}$$

where, σ_a is the stress amplitude, N_f is the number of cycles to failure, and C_1 and C_2 are the material constants that are typically obtained from the experiments. In the revised Basquin equation, the function $f(R_a)$ is the correction term to account for the stress concentrations due to the roughness surface.

The parameters of the proposed model were identified using the least squares regression method. The dataset was divided into calibration (70%) and validation (30%) subsets for model development and evaluation. The accuracy of the proposed model in the fatigue life prediction is assessed using the coefficient of determination and the root mean square error (RMSE).

3. RESULTS

3.1 Surface roughness characterization

3.1.1 Surface roughness parameters

Differences in surface roughness were observed between the six surface states examined, as shown in Table 1. The lowest values of arithmetic average surface roughness were recorded for mirror-polished surfaces (S1), with Ra = 0.05 µm, and the highest values were recorded for chemically etched surfaces (S6), with Ra = 2.01 µm.

In addition, the progression of supplementary surface roughness parameters Rq, Rz, Rsk, and Rku, as shown in Table 1, also demonstrated similar monotonic trends with respect to an increase in Ra.

3D surface topography measurements are shown in Figure 1. The mirror-polished surface (S1) exhibits a nearly flat morphology, whereas the chemically etched surface (S6) shows pronounced peaks and valleys.

Table 1. Surface roughness parameters of test specimens

Sample ID	Surface Treatment	Ra (µm)	Rz (µm)	Rq (µm)	Rsk (Skewness)	Rku (Kurtosis)
S1	Mirror polished	0.05	0.42	0.06	-0.12	3.21
S2	Fine polished	0.18	0.92	0.22	-0.05	2.98
S3	Standard polished	0.45	2.15	0.52	0.08	2.76
S4	Fine ground	0.85	3.76	0.97	0.21	2.64
S5	Coarse ground	1.42	7.24	1.61	0.34	2.51
S6	Chemically etched	2.01	9.18	2.23	0.46	3.05

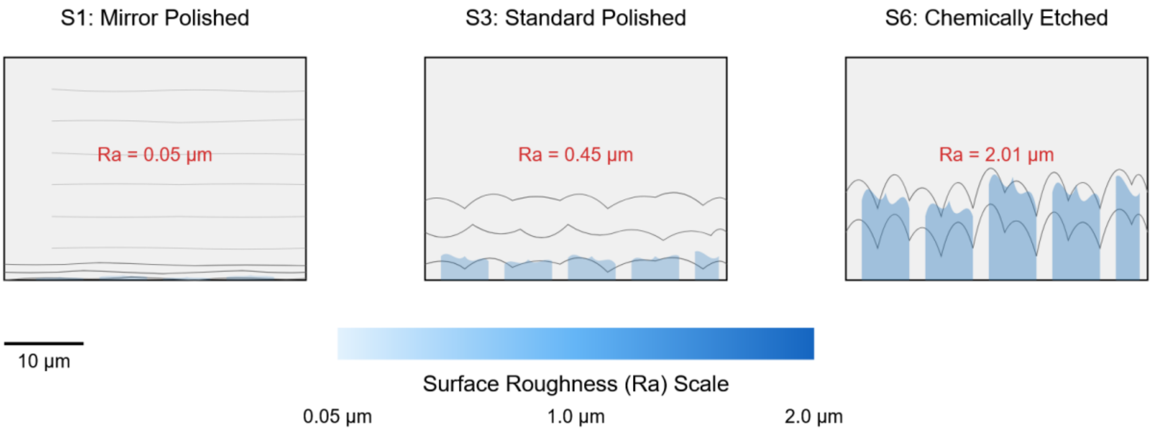

AFM topographic profiles showing the progressive increase in surface roughness from mirror polished (S1) to standard polished (S3) to chemically etched (S6) conditions.

Figure 1. 3D topographic image of surface condition

3.1.2 Microstructural analysis

Microstructural analysis was carried out using scanning electron microscopy and electron backscatter diffraction (EBSD). Based on the analysis, it is found that variations in near surface deformation features exist for various surface conditions, and deformation is found to be pronounced for specimens S4 and S5.

XRD analysis results indicate that specimens S4 and S5 contain strain-induced α′ martensite, and this phase transformation is not found for other surface conditions.

3.2 Mechanical properties

3.2.1 Tensile behavior

The tensile properties of ultrathin sheets of 304 stainless steel conditions are presented in Table 2, showing a systematic reduction in yield strength, UTS, and ductility is observed with increasing surface roughness (Ra). In the present study, the yield strength reduces from 325 MPa, as observed in the case of the mirror-polished surface (S1), to 270 MPa, as observed in the case of the chemically etched surface (S6), showing a reduction of about 17%. Similarly, the UTS reduces from 698 MPa to 622 MPa, showing a reduction of about 11%.

The stress-strain curves for the various surface conditions are as shown in Figure 2. The curves exhibit typical elastic–plastic behavior with strain hardening. A progressive downward shift of the curves is observed with increasing surface roughness.

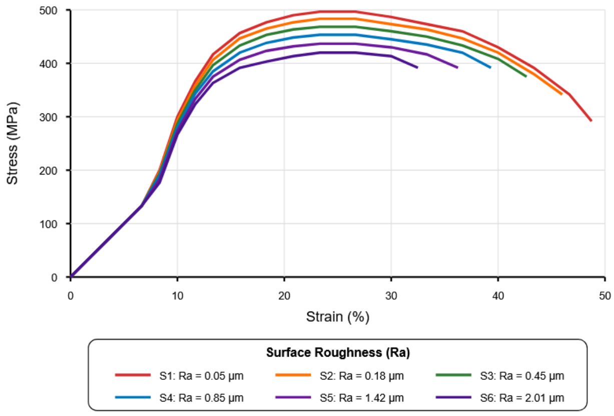

Figure 2. Stress-strain curves for different surface roughness conditions

Table 2. Mechanical properties of 304 SS sheets with different surface roughness values

Sample ID	Ra (μm)	Yield Strength (MPa)	UTS (MPa)	Elongation (%)	Hardness (HV)
S1	0.05	325	698	45.3	182
S2	0.18	318	685	44.2	178
S3	0.45	307	671	42.8	175
S4	0.85	293	654	40.1	171
S5	1.42	281	638	38.5	168
S6	2.01	270	622	36.2	165

Note: UTS: ultimate tensile strength

Table 3. Fatigue test results at different surface roughness levels

Sample ID	Ra (μm)	Fatigue Limit at 10^7 Cycles (MPa)	Fatigue Ratio (Fatigue Limit/UTS)	Fatigue Crack Initiation Site
S1	0.05	325	0.465	Subsurface inclusions
S2	0.18	310	0.452	Subsurface inclusions/Surface
S3	0.45	285	0.425	Surface irregularities
S4	0.85	258	0.394	Surface valleys
S5	1.42	235	0.368	Surface peaks/valleys
S6	2.01	210	0.338	Surface peaks

Note: UTS: ultimate tensile strength

The strain hardening exponent (n) decreases from 0.42 for S1 to 0.37 for S6. Total elongation also decreases from 45.3% to 36.2% with increasing surface roughness.

3.2.2 Fatigue behavior

The fatigue properties showed even higher dependence on surface roughness than the tensile properties. Table 3 shows the results of the fatigue test for the 6 surface conditions. The fatigue limit at 10^7 cycles reduced from 325 MPa for the mirror-polished specimens (S1) to 210 MPa for the chemically etched specimens (S6), indicating a significant decrease of about 35%.

A significant relationship between surface roughness and fatigue was established, although the results should be interpreted in the context of the small number of surface conditions.

3.3 Fractography and failure mechanisms

3.3.1 Tensile fracture

Tensile specimen fracture surfaces were mostly characterized as ductile for all surface roughness conditions, but different in the location of the fracture initiation. In the mirror-polished (S1) and fine-polished (S2) samples, an onset of specimen (er) fracture at multiple locations within the cross-section is observed, without discriminating between the superficial and the understerial location. On the other hand, with increasing surface roughness (S3-S6), specimens were found to initiate fracture through surface irregularities especially at sharp notch like features (Figure 3).

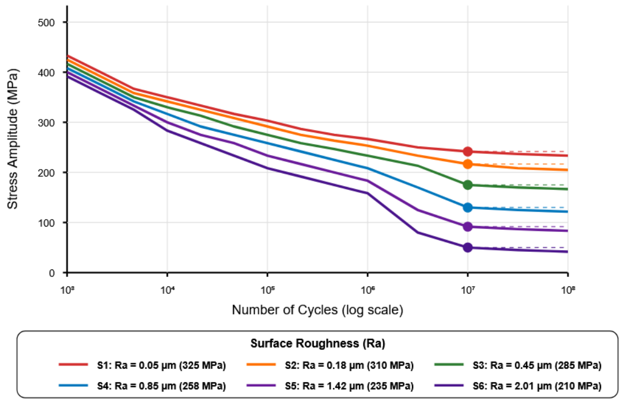

Figure 3. S-N curves for different surface roughness conditions

The reduced area at fracture decreased with increasing surface roughness, ranging from 65% for S1 to 48% for S6, in similar trend with the reduction of the elongation at fracture. For S1 and S2 specimens, the dimple size and distribution of the fracture surfaces was more uniform, while fracture surfaces of S3–S6 specimens displayed more heterogeneous dimple structures.

3.3.2 Fatigue fracture

Scanning electron microscope (SEM) analysis of the fatigue fracture surfaces (Figure 4) shows a change in the crack initiation location with increasing surface roughness. For smooth specimens (S1), fatigue crack initiation occurs at subsurface inclusions, and the fracture surfaces exhibit characteristic fish-eye features.

As the surface roughness increases, the crack initiation location changes toward surface. In specimens with higher roughness (S3–S6), fatigue cracks are observed to initiate at surface irregularities such as valleys and peaks (Figure 5).

The fracture surfaces also show differences in morphology between smooth and rough conditions, particularly near the crack initiation regions.

The mechanism map in Figure 6 shows the fatigue regimes of crack initiation in terms of surface features and stress amplitude.

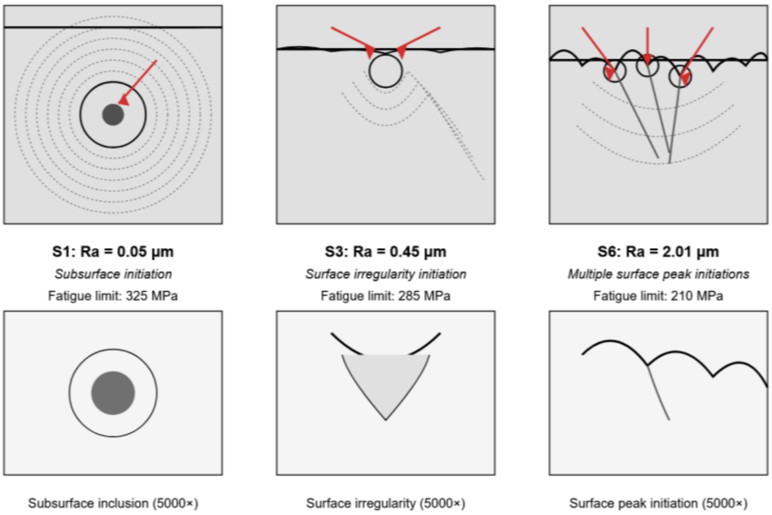

Figure 4. Scanning electron microscope (SEM) fractography of fatigue test specimens

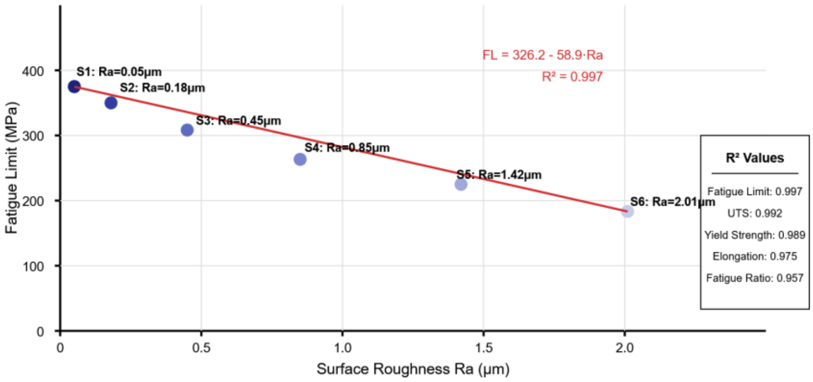

Figure 5. Surface roughness vs. mechanical properties

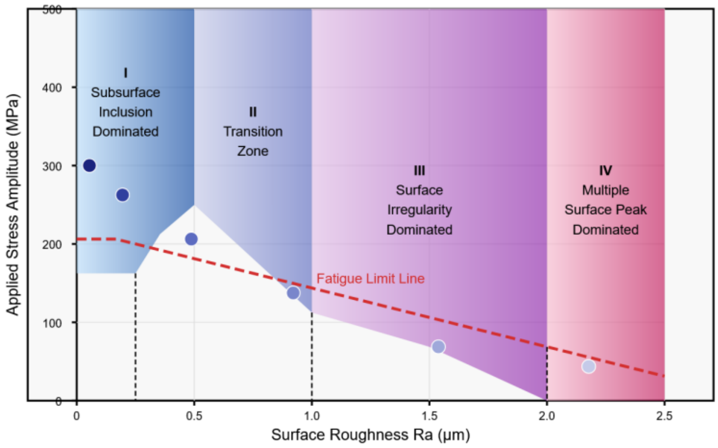

Figure 6. Mechanism map of fatigue crack initiation

3.3.3 Crack propagation characteristics

The fatigue crack growth regions show different propagation characteristics depending on the surface roughness. In the case of low surface roughness specimens (S1 and S2), the crack propagation was dominated by TN mode with plain fatigue striations seen at higher magnifications.

As the cracks propagate from the point of initiation, the spacing of the fatigue striations increases.

For the specimens with higher surface roughness (S3 to S6), the fatigue crack propagation characteristics in the initial propagation region exhibit a non-uniform path, with a mixture of transgranular and intergranular fracture modes. The crack path in this region is more non-uniform near the surface.

As the cracks move away from the surface, the fatigue crack propagation characteristics exhibit a uniform pattern, with a predominantly transgranular mode of fracture. The spacing of the fatigue striations, evaluated from the same distance from the fatigue crack initiation point, indicates similar values for the various surface roughness specimens.

3.4 Finite element analysis and stress concentration effects

FEA was employed to measure the impact of surface roughness on the stress concentration factor. The acquired surface profiles were utilized in the finite element model to replicate the stress distribution under specified loading conditions. A two-dimensional plane strain FE model was created to simulate the effect of the surface features on the local value of the stress concentration factor.

From the FE results, it is observed that the value of the stress concentration factor is significantly affected by the surface roughness. For the mirror-polished surfaces S1. The value of the stress concentration factor (Kt) is approximately 1.03 for the mirror-polished surfaces S1. On the other hand, the value of Kt is approximately 1.78 for the chemically etched surfaces S6.

Regression analysis was used to determine the relationship between the surface roughness parameters and the calculated value of the stress concentration factor. It is observed that the maximum height parameter has a better correlation with the value of the Kt compared with the arithmetic average parameter.

The relationship between the value of the stress concentration factor and the surface roughness is given by the equation:

$$Kt = 1 + \alpha \left(\frac{Rz}{t}\right)^{\beta} \tag{2}$$

The calculated Kt values obtained from the FEA follow the same trend as the empirical relationship given in Eq. (2).

To further investigate the effect of 3D surface morphology, 3D finite element models were created from the measured surface topography for the selected surface conditions. The results show that the 3D model has slightly higher values of stress concentration compared to the two-dimensional model. The difference is around 5-10%.

The two-dimensional model represents a simplified form of the actual 3D surface morphology. The difference between the 2D and 3D results is approximately 5–10%. The stress distribution near complex surface features appears more localized, and the calculated values are considered approximate.

3.5 Predictive model for fatigue life

Based on the experimental results and the FEA, a fatigue life prediction model is proposed, considering the effects of surface roughness on the fatigue life of ultra-thin 304 stainless steel sheets. This model is a modified version of the classical Basquin equation, in which the effect of surface-induced stress concentration is incorporated. The modified equation is expressed as:

$$\sigma_a = \mathrm{C}_1 N_f^{-\mathrm{C}_2}[1 - \mathrm{C}_3 Ra^{\mathrm{C}_4}] \tag{3}$$

In the above equation, σ_a is the stress amplitude, N_f is the number of cycles to failure, Ra is the arithmetic average surface roughness, and t is the sheet thickness. C_1, C_2, C_3, and C_4 in the equation are material-dependent constants.

Using the least squares regression technique, the values of the constants in the equation were determined using the experimental S-N curves. For the material under investigation, 0.2 mm thick 304 stainless steel sheets, the values of the constants in the equation were found to be $C_1 = 850$ MPa, $C_2 = 0.085$, $C_3 = 0.18$, and $C_4 = 0.52$.

A comparison between the predicted fatigue life and the experimental data across the different surface conditions is presented. A strong correlation between the predicted and experimental fatigue life is observed, particularly in the high-cycle fatigue region $N_f > 10^5$.

The inclusion of the term related to surface roughness in the suggested model accounts for the effect of surface irregularities on stress concentration, as quantified in the FEA by the stress concentration factor (Kt). It is a combined effect of surface roughness and stress concentration.

The accuracy of the proposed model is limited to the range of surface conditions and loading parameters investigated in this work. The relatively limited number of surface states and experimental results is considered.

4. DISCUSSION

The present results should be interpreted with caution, as surface roughness is not the only varying parameter among the investigated conditions. The different surface preparation techniques (polishing, grinding, and chemical etching) may also introduce variations in near-surface microstructure, including plastic deformation, residual stress, and strain-induced martensitic transformation. Therefore, the observed trends reflect a combined effect of surface geometry and metallurgical condition, rather than roughness alone.

4.1 Effect of surface roughness on tensile behavior

The tensile properties of ultrathin 304 stainless steel sheets demonstrate a dependency on surface roughness. As Ra increases, yield strength, UTS, and ductility decrease. Yield strength decreases from 325 MPa to 270 MPa, and UTS decreases from 698 MPa to 622 MPa. Elongation decreases from 45.3% to 36.2% as surface conditions change from mirror-polished (S1) to chemically etched (S6).

The decrease in tensile properties is attributed to surface irregularities, where geometrical discontinuities produce high stress concentrations on rough surfaces. Deformations occurring near the surface during surface preparation also play a role. The presence of strain-induced martensite in specimens

S4 and S5 indicates that subsurface deformation is present in these conditions.

Similar behavior has been reported for thin metallic sheets subjected to different surface treatments [9-12].

4.2 Effect of surface roughness on fatigue behavior

The fatigue properties show a higher dependence on surface roughness compared to tensile properties. It is noted that the fatigue limit decreases from 325 MPa for mirror-polished specimens (S1) down to 210 MPa for chemically etched specimens (S6).

This trend is in accordance with the notion that fatigue properties are more sensitive to surface finish than static mechanical properties, as has been consistently shown in fatigue tests of metal materials [13-15, 20]. The increased sensitivity can be attributed to the fact that fatigue crack initiation is a localized phenomenon that is strongly influenced by surface irregularities acting as stress concentrators. A strong decreasing trend between surface roughness and fatigue limit is observed. However, this relationship should be interpreted carefully due to the limited number of surface conditions and possible experimental scatter. Consequently, rather than being a strictly deterministic link, the observed correlation reflects a general trend.

This indicates that the observed behavior is influenced by both surface roughness and subsurface microstructural changes.

4.3 Fatigue crack initiation mechanisms

SEM analysis of the fatigue fracture surface reveals a change in the mechanism of crack initiation for fatigue as surface roughness increases. In the case of smooth specimens (S1), crack initiation occurs at subsurface inclusions, and the fracture surface has characteristic features of a fish eye, as observed in earlier work on high-cycle fatigue of steel [16-19].

As surface roughness increases, the crack initiation mechanism becomes more and more surface-related. For rough specimens (S3, S6), crack initiation for fatigue occurs at surface features, which act as stress raisers.

It should be noted that the change in the crack initiation mechanism is a continuous process, and intermediate surface roughness values may show a combination of both surface and subsurface-related crack initiation mechanisms.

4.4 Stress concentration and finite element analysis

FEA confirms that surface roughness has a significant effect on stress concentration. The stress concentration factor (Kt) increases from approximately 1.03 for smooth surfaces to 1.78 for rough surfaces. This indicates that surface roughness acts as a major geometric stress raiser. From the results, it is observed that the maximum height parameter Rz shows a stronger correlation with Kt compared to Ra. This indicates that the peak-to-valley features have a larger effect on the stress concentration. This is in accordance with previous research work [14, 15].

Although the 2D model provides a simplified representation of surface roughness, additional 3D simulations show only a 5-10% increase in Kt values. This suggests that the 2D approach provides a reasonable approximation for evaluating general trends, although local stress states may be more complex.

4.5 Crack propagation behavior

Analysis of the fatigue crack growth regions shows that surface roughness influences crack initiation and early crack growth. Specimens that had smoother surfaces had crack growth that was transgranular, and the crack exhibited distinct fatigue striations. On the other hand, specimens that had rough surfaces had irregular crack paths, especially near the surface.

Away from the surface, the effect of surface roughness is seen to decrease as the crack grows further. The similarity in striation spacing under various conditions suggests that long crack growth is independent of surface conditions.

4.6 Engineering implications

The results indicate that surface conditions have a considerable effect on the fatigue response of ultra-thin 304 stainless steel sheets. It is generally recognized that smoother surfaces improve the fatigue response by reducing stress concentrations and delaying crack initiation.

The suggested values of surface roughness should, however, be considered to be indicative for the material and conditions investigated. It is possible that the suggested values may need to be adjusted for other materials, conditions, and environments.

In summary, the results offer a view of the combined effect of surface roughness and microstructure on the material and fatigue response.

5. CONCLUSION

In this study, the influence of surface roughness on the mechanical and fatigue behavior of ultra-thin 304 stainless steel sheets were investigated. The results indicate that surface roughness has an influence on the static and fatigue behavior of the material.

When the arithmetic average roughness varies from 0.05 to 2.01 μm, the yield strength and UTS of the material decrease by approximately 17% and 11%, respectively, whereas the total elongation of the material reduces by approximately 20%. The fatigue behavior of the material indicates a higher sensitivity to surface roughness, where the fatigue limit varies from 325 to 210 MPa, which indicates a reduction of approximately 35%. A decreasing trend between fatigue limit and surface roughness is observed.

Fractography analysis shows a change in the fatigue crack initiation mechanism with increasing surface roughness. For lower roughness values, crack initiation occurs at subsurface inclusions, while for higher roughness values, crack initiation is observed at surface irregularities.

FEA shows that surface roughness influences stress concentration. The stress concentration factor (Kt) increases from approximately 1.03 to 1.78 as the surface roughness increases from 0.05 to 2.01 μm.

A fatigue mechanism map is developed to describe crack initiation behavior as a function of surface roughness and applied stress. The results indicate that surface roughness has a positive effect on fatigue, especially when surface roughness is below 0.2 μm.

REFERENCES

[1] Gadelmawla, E.S., Koura, M.M., Maksoud, T.M.A.,

Elewa, I.M., Soliman, H.H. (2002). Roughness parameters. Journal of Materials Processing Technology, 123(1): 133-145. https://doi.org/10.1016/S0924-0136(02)00060-2

[2] Thomas, T.R. (2013). Roughness and function. Surface Topography: Metrology and Properties, 2(1): 014001. https://doi.org/10.1088/2051-672X/2/1/014001

[3] Petropoulos, G.P., Pandazaras, C.N., Davim, J.P. (2010). Surface texture characterization and evaluation related to machining. In: Davim, J.P. (eds) Surface Integrity in Machining. Springer, London, pp. 37-66. https://doi.org/10.1007/978-1-84882-874-2_2

[4] Whitehouse, D.J. (2010). Handbook of Surface and Nanometrology, 2nd ed. CRC Press, Boca Raton. https://doi.org/10.1201/9781420034196

[5] Leach, R. (2013). Characterisation of Areal Surface Texture. Springer, Berlin. https://doi.org/10.1007/978-3-642-36458-7

[6] De Chiffre, L., Lonardo, P.M., Trumpold, H., Lucca, D.A., Goch, G., Brown, C.A., Raja, J., Hansen, H.N. (2000). Quantitative characterisation of surface texture. CIRP Annals, 49(2): 635-652. https://doi.org/10.1016/S0007-8506(07)63458-1

[7] Blunt, L., Jiang, X. (2003). Advanced Techniques for Assessment Surface Topography: Development of a Basis for 3D Surface Texture Standards "Surfstand". Elsevier.

[8] Jiang, X., Whitehouse, D.J. (2012). Technological shifts in surface metrology. CIRP Annals, 61(2): 815-836. https://doi.org/10.1016/j.cirp.2012.05.009

[9] Salehi, A., Sprejz, S., Ruehl, H., Olayioye, M., Cattaneo, G. (2024). An imprint-based approach to replicate nano- to microscale roughness on gelatin hydrogel scaffolds: Surface characterization and effect on endothelialization. Journal of Biomaterials Science, Polymer Edition, 35(8): 1214-1235. https://doi.org/10.1080/09205063.2024.2322771

[10] Novovic, D., Dewes, R.C., Aspinwall, D.K., Voice, W., Bowen, P. (2004). The effect of machined topography and integrity on fatigue life. International Journal of Machine Tools and Manufacture, 44(2-3): 125-134. https://doi.org/10.1016/j.ijmachtools.2003.10.018

[11] Chen, X., Yan, J., Karlsson, A.M. (2014). On the determination of residual stress and mechanical properties by indentation. Materials Science and Engineering: A, 574: 117-126. https://doi.org/10.1016/j.msea.2014.06.114

[12] Wang, C., Guo, Z., Zhou, B., Li, B., Fei, S., Deng, H., Shen, G. (2024). Experimental investigation and numerical study on evolution of surface roughness caused by ultrasonic shot peening of 2024 aluminum alloy sheet. Journal of Materials Research and Technology, 30: 9061-9083. https://doi.org/10.1016/j.jmrt.2024.05.254

[13] Suraratchai, M., Limido, J., Mabru, C., Chieragatti, R. (2008). Modelling the influence of machined surface roughness on the fatigue life of aluminium alloy. International Journal of Fatigue, 30(12): 2119-2126. https://doi.org/10.1016/j.ijfatigue.2008.06.003

[14] Arola, D., Williams, C.L. (2002). Estimating the fatigue stress concentration factor of machined surfaces. International Journal of Fatigue, 24(9): 923-930. https://doi.org/10.1016/S0142-1123(02)00012-9

[15] As, S.K., Skallerud, B., Tveiten, B.W., Holme, B. (2008). Fatigue life prediction of machined components using finite element analysis of surface topography. International Journal of Fatigue, 30(10-11): 1836-1845. https://doi.org/10.1016/j.ijfatigue.2005.07.031

[16] Niu, X., He, C., Zhu, S.P., Foti, P., Berto, F., Wang, L., Wang, Q. (2024). Defect sensitivity and fatigue design: Deterministic and probabilistic aspects in AM metallic materials. Progress in Materials Science, 144: 101290. https://doi.org/10.1016/j.pmatsci.2024.101290

[17] Li, X., Liu, C., Wang, X., Dai, Y., Zhan, M., Liu, Y., Wang, Q. (2024). Effect of microstructure on small fatigue crack initiation and early propagation behavior in super austenitic stainless steel 654SMO. International Journal of Fatigue, 179: 108022. https://doi.org/10.1016/j.ijfatigue.2023.108022

[18] Mughrabi, H. (2013). Microstructural fatigue mechanisms: Cyclic slip irreversibility, crack initiation, non-linear elastic damage analysis. International Journal of Fatigue, 57: 2-8. https://doi.org/10.1016/j.ijfatigue.2012.06.007

[19] Murakami, Y., Nomoto, T., Ueda, T. (1999). Factors influencing the mechanism of superlong fatigue failure in steels. Fatigue & Fracture of Engineering Materials & Structures, 22(7): 581-590. https://doi.org/10.1046/j.1460-2695.1999.00187.x

[20] Chan, K.S. (2010). Roles of microstructure in fatigue crack initiation. International Journal of Fatigue, 32(9): 1428-1447. https://doi.org/10.1016/j.ijfatigue.2009.10.005

[21] Nashed, M.S., Mohamed, M.S., Shady, O.T., Renno, J. (2022). Using probabilistic neural networks for modeling metal fatigue and random vibration in process pipework. Fatigue & Fracture of Engineering Materials & Structures, 45(4): 1227-1242. https://doi.org/10.1111/ffe.13660

[22] Fan, Z., Yu, X., Zhang, Q., He, S., Chen, G., Du, J., Wen, Y. (2018). Fatigue life estimation for simply-supported pipeline of robots under hybrid excitation. International Journal of Fatigue, 108: 127-139. https://doi.org/10.1016/j.ijfatigue.2017.11.002

[23] Yang, J., Li, B., Wang, K., Zhao, L., Xu, L., Chen, X. (2024). Cyclic deformation behavior and damage mechanism of 316H stainless steel under low-cycle fatigue loading at 650 ℃. International Journal of Fatigue, 188: 108523. https://doi.org/10.1016/j.ijfatigue.2024.108523

[24] Ding, B., Du, J., Wang, J. (2024). Interface shearing promoted plastic flow instability of nanolaminated composites. International Journal of Mechanical Sciences, 270: 109114. https://doi.org/10.1016/j.ijmecsci.2024.109114

[25] Lo, K.H., Shek, C.H., Lai, J.K.L. (2009). Recent developments in stainless steels. Materials Science and Engineering: R: Reports, 65(4-6): 39-104. https://doi.org/10.1016/j.mser.2009.03.001

[26] Radojković, B., Jegdić, B., Pejić, J., Eraković Pantović, S., Marunkić, D., Simović, A., Alić, B. (2024). Passive film properties and corrosion resistance of AISI 304L stainless steel. Corrosion Engineering, Science and Technology, 60(4): 233-249. https://doi.org/10.1177/1478422X241286297

[27] Lee, S.M., Lee, W.G., Kim, Y.H., Jang, H. (2012). Surface roughness and the corrosion resistance of 21Cr ferritic stainless steel. Corrosion Science, 63: 404-409.

https://doi.org/10.1016/j.corsci.2012.06.031

[28] Shahryari, A., Omanovic, S., Szpunar, J.A. (2008). Electrochemical formation of highly pitting resistant passive films on a biomedical grade 316LVM stainless steel surface. Materials Science and Engineering: C, 28(1): 94-106. https://doi.org/10.1016/j.msec.2007.09.002

[29] Scott, S., Atwater, M. (2024). New method for position and energy controlled surface mechanical attrition treatment and its effects in 304 stainless steel. Journal of Materials Science, 59(4): 1679-1698. https://doi.org/10.1007/s10853-023-09274-w

[30] Ye, C., Telang, A., Gill, A.S., Suslov, S., Idell, Y., Zweiacker, K., Wiezorek, J.M.K., Zhou, Z., Qian, D., Mannava, S.R., Vasudevan, V.K. (2014). Gradient nanostructure and residual stresses induced by ultrasonic nano-crystal surface modification in 304 austenitic stainless steel for high strength and high ductility. Materials Science and Engineering: A, 613: 274-288. https://doi.org/10.1016/j.msea.2014.06.114

[31] Zhao, H., Ma, X., Wang, Z., Jiang, Z., Zhou, C., Zhao, J. (2024). Surface roughness evolution and heterogeneous plastic deformation of austenitic stainless steel during micro deep drawing: Modeling and experiment. International Journal of Plasticity, 176: 103964. https://doi.org/10.1016/j.ijplas.2024.103964

NOMENCLATURE

E	Young’s modulus, GPa
FL	Fatigue limit, MPa
FR	Fatigue ratio (FL / UTS)
Kt	Stress concentration factor
Nf	Number of cycles to failure, cycles
Ra	Arithmetic average surface roughness, μm
Rq	Root mean square roughness, μm
Rz	Maximum height of surface profile, μm
Rsk	Surface skewness
Rku	Surface kurtosis
Sa	Areal arithmetic mean height, μm
Sq	Areal root mean square height, μm
Sz	Maximum areal height, μm
t	Sheet thickness, mm
UE	Uniform elongation, %
UTS	Ultimate tensile strength, MPa
YS	Yield strength (0.2% offset), MPa

Greek symbols

σ_a	Stress amplitude, MPa
α	Empirical coefficient (stress concentration model)
β	Empirical exponent (stress concentration model)

Subscripts

a	Stress amplitude
f	Fatigue
max	Maximum
min	Minimum
$-C_2$	Basquin fatigue exponent
C_4	Roughness sensitivity exponent